Check for updates

Uniformity, performance, and durability of roll-to-roll-coated iridium oxide electrolyzer catalyst layers

Scott A. Mauger, [ID] *[a] Sanghun Lee,†[a] Robin Rice,[a] Elliot Padgett,[a] Sarah Zaccarine,‡[b] Maryam Ahmadi,[c] Mariah Batool,[c] Kimberly S. Reeves,[d] David A. Cullen, [ID] [d] Svitlana Pylypenko,[b] Jasna Jankovic[c] and Michael Ulsh[a]

This work investigates the use of roll-to-roll coating methods for the production of iridium oxide catalyst layers for proton exchange membrane water electrolyzers. Catalyst layers were produced using two coating methods: slot die and gravure. By varying the solids content of the catalyst ink and coating process variables loadings between 0.08 and 0.64 mg_{Ir} cm^{-2} were prepared with relatively high spatial uniformity. However, at loadings below 0.2 mg_{Ir} cm^{-2} microscopy reveals voids in the catalyst layer due to similar length scales of catalyst agglomerates and overall layer thickness. Electrochemical testing shows that these voids do not impact initial membrane electrode assembly performance but lead to increased performance losses after potential cycling compared to spray coated catalyst layers.

Introduction

Water electrolyzers efficiently generate hydrogen through electrochemical water splitting. While there are multiple types of electrolyzers, proton exchange membrane water electrolyzers (PEMWEs) are of interest because they can operate at low temperatures and readily operate intermittently.[1] To achieve greater adoption of PEMWE, stack cost reductions are needed to reduce hydrogen production costs.[2] One approach to reduce hydrogen production costs is *via* increases in system efficiency is though advances in membranes, porous transport layers (PTLs), and catalysts that reduce resistive losses or improve catalyst utilization and durability.[3] A complementary approach is to reduce materials costs. For PEMWE systems, the anode catalyst layer contains iridium or iridium oxide catalyst particles, which account for a significant portion of membrane electrode assembly materials costs due to the high price of iridium.[4] Currently-fielded systems typically have anode

loadings greater than 1 mg_{Ir} cm^{-2} with near and long-term targets of 0.4 and 0.1 mg_{Ir} cm^{-2}, respectively.[2,3] Previous work has shown high PEMWE performance is possible with ultra-low Ir loadings (< 0.2 mg_{Ir} cm^{-2}) using ultrasonic spray coating.[5]

Additionally, significant cost reductions may be realized from advances in manufacturing and economies of scale.[2] Pairing improvements in system efficiency and materials costs with a reduction in production costs is needed to achieve system and hydrogen cost targets. To accomplish this, it is critical to understand the ability of manufacturing methods to produce future generation systems. Roll-to-roll (R2R) coating methods are envisioned for catalyst layer production as they can be highly automated and are capable of producing material at linear rates of m s^{-1}, in some cases.[6] In contrast to the spray coating processes mentioned above, which used a dilute catalyst ink (0.08 wt% solids), most R2R coating methods use catalyst inks with higher solids concentrations. Published work on slot-die coated (R2R and sheet) anodes have used inks with over 20 wt% IrO_2 to obtain loadings over 1 mg_{Ir} cm^{-2}.[7,8] To meet near-term and future hydrogen cost targets, R2R processes will need to be developed that can achieve favorable performance and degradation at anode loadings below 0.5 mg_{Ir} cm^{-2} in the near term and 0.1 mg_{Ir} cm^{-2} in the long term.[2] This requires a thorough examination of coating methods to address processing challenges and ultimately produce these low-loaded catalyst layers with high quality and without sacrificing performance or durability.[5]

R2R coating encompasses many coating methods including slot die, gravure, flexography, offset, and slide coating.[9] For each

[a] *National Laboratory of the Rockies, Golden, Colorado, USA.*
  E-mail: scott.mauger@nlr.gov
[b] *Department of Chemistry, Colorado School of Mines, Golden, Colorado, USA*
[c] *Center for Clean Energy Engineering, Institute of Materials Science, and Materials Science and Engineering Department, University of Connecticut, Storrs, CT, USA*
[d] *Center for Nanophase Materials Sciences, Oak Ridge National Laboratory, Oak Ridge, TN 37831, USA*
† Current address: Department of Climate and Energy Systems Engineering, Ewha Womans University, 52 Ewhayeodae-gil, Seodaemun-gu, Seoul, 03760, Republic of Korea.
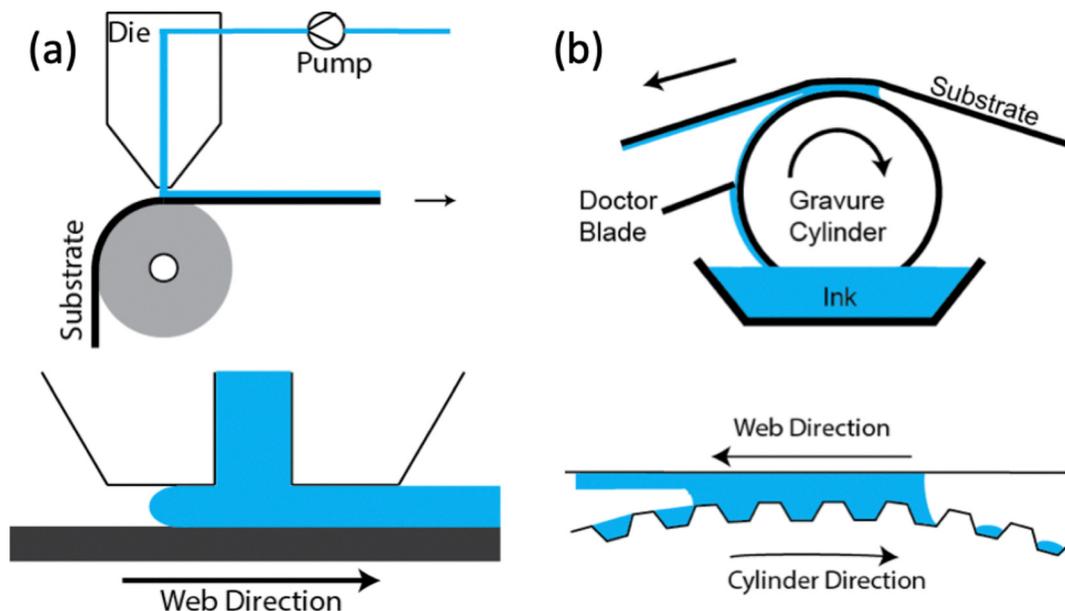‡ Current address: Physical Electronics, Chanhassen, Minnesota, USA.

Fig. 1 Schematics of (a) slot die coating and (b) reverse gravure coating.

method, a liquid coating containing dissolved and/or suspended solids (catalyst and ionomer in the case of PEMWE) is applied to a substrate and then solidified in a subsequent step. Despite this similarity, each method comprises a unique modality to apply the coating, and as such has unique considerations for optimal coating properties, process requirements, and final product specifications.

For example, and as shown in Fig. 1, slot-die coating involves the application of a liquid to a substrate from a narrow channel fed at a known flow rate, while gravure coating involves the transfer of liquid from a rotating, patterned cylinder onto a substrate that is either tensioned over the gravure cylinder (shown) or supported by an elastic backing roll (not shown). One of the primary advantages of slot die coating is that it is a pre-metered coating method where the film thickness is controlled by the flow rate of the coating fluid and the substrate speed. This enables facile control of the film thickness within an upper and lower bounding flow rate for a given web speed, which defines the coating window.[6]

In contrast, gravure coating is not a pre-metered method. To apply the coating, the gravure cylinder rotates through a pan of the coating fluid, filling the engraving with the fluid. A doctor blade is used to remove excess fluid from the gravure cylinder surface. It has been found that doctoring is more easily achieved with low viscosity fluids like the catalyst inks used in this work.[10] It is also well suited for coating thin films.[11] The coating thickness is largely controlled by the engraved volume of the gravure cylinder, known as the volume factor, which is reported in $m^3\ m^{-2}$. However, not all the fluid within the engraving is transferred from the gravure cylinder to the substrate. The fraction of fluid transferred, known as pickout, is controlled by coating process parameters,[12] fluid properties,[13] and cylinder patterning,[14] which additionally influence coating thickness.

The fluid mechanics governing each coating method give rise to an operating window that is determined by the coating modality (*e.g.*, slot *versus* gravure) process specifications (*e.g.*, web speed, equipment geometry, liquid film thickness) and fluid properties (rheology, density, and surface tension). Within the operating window, defect-free coatings can be obtained. Outside the operating window several types of defects can occur.[15–18] For slot-die coating, the coating window boundaries are the low-flow and high-flow limits. The low-flow limit is the lowest flow rate where a defect-free coating can be obtained at a given web speed.[16,19] Below this flow rate, the coating bead between the die and substrate becomes unstable or breaks, leading to several types of defects including ribbing or uncoated patches. On the other extreme is the high-flow limit, which is the maximum flow rate where the coating bead is stable. Above the high-flow limit, the upstream meniscus extends beyond the length of the up-steam die lip face and leads to a phenomenon known as weeping or dripping where liquid flows out of the upstream meniscus and metering of the fluid is lost. The coating window is dependent on many factors including die geometry, fluid properties, and process conditions.[6,16] In gravure, like slot die, flow instabilities in the coating bead can lead to ribbing and other defects. A defect known as flashing, where sections of the substrate are uncoated may arise from improper pick-out.

In this study, slot die and gravure coating were utilized for R2R fabrication of anode catalyst layers for PEMWEs. Through variation of the coating process conditions and catalyst ink concentration, we were able to explore the range of loadings obtainable for given process conditions. These catalyst layers were fabricated into MEAs for performance and durability comparisons. Overall, we see little impact of the coating method on initial performance, even at loadings near $0.2\ mg\ cm^{-2}$. However, in accelerated stress testing we observe

that microstructural differences in coating uniformity dramatically influence durability.

Materials and methods

Ink preparation and characterization

The R2R anode catalyst inks were prepared using a commercial IrO$_2$ catalyst (Alfa Aesar, Premion, minimum 85% oxide) and Nafion D2020 ionomer dispersion (20% ionomer, 34% water, 46% 1-propanol, 920 EW). The inks were prepared by the sequential addition of IrO$_2$ powder, water, 1-propanol, and ionomer dispersion into a glass jar. For safety, it is critical that the iridium oxide catalyst is fully wetted with water prior to the addition of 1-propanol and ionomer dispersion. Three inks containing 10, 20, or 30 wt% IrO$_2$ (with respect to the solvent mass) were prepared for this study. For all inks, the ionomer-to-catalyst ratio was 0.2 (w/w). The 20 and 30 wt% inks were prepared with a water : 1-propanol ratio of 1 : 1 (w : w). For the 10 wt% ink, a water : 1-propanol ratio of 1 : 3 (w : w) was used because de-wetting from the substrate occurs at higher water content. The inks were dispersed using a high-shear rotor-stator mixer (Ika Turrax SN-25, using an 18G mixing head) at a speed of 10 000 rpm for 15 min. Following dispersion, the inks were stirred overnight with a magnetic stir bar to allow for degassing. The same inks were used for slot die and gravure coating.

For spray-coated catalyst layers dilute inks were used. The cathode catalyst was a 50 wt% Pt on high surface area carbon (Tanaka Kikinzoku Kogyo, TEC10E50E). The cathode spray ink had a concentration of 2 mg mL^{-1} in a mixture of DI water and n-propyl alcohol (nPA) at a mass ratio of 1 : 0.61 (water : nPA). The ionomer to carbon weight ratio of 0.45 : 1. The ink was pre-chilled with ice and mixed for 30 s in a probe ultrasonicator, followed by 15 min in an ice-water filled bath ultrasonicator. The catalyst was dispersed in a water/n-propanol mixture with the same ratio as the cathode catalyst ink. The concentration of the iridium oxide anode ink was of 2.75 mg$_{Ir}$ mL^{-1} with an ionomer to catalyst mass ratio of 0.2 : 1. The ink was pre-chilled with ice and mixed for 2 min in a probe ultrasonicator, followed by 30 min in an ice-water-filled bath ultrasonicator.

The steady-shear viscosities of the catalyst inks were measured using a stress-controlled rheometer (Thermo Scientific HAAKE MARS 60) with a parallel plate geometry (35 mm) and a 500 µm gap. The temperature was held constant at 25 °C using a liquid-cooled Peltier plate. Prior to measurement, inks were pre-sheared at 500 s^{-1} for 1 min to remove any loading history. The steady-shear viscosities were then measured in a decreasing rate sweep from 500–1 s^{-1}.

Roll-to-roll coating

The R2R coating line (MiniLabo Deluxe, Yasui Seiki) consists of the coating station followed by two air convection ovens (Fig. S1). The roll of substrate is secured at either end of the coating and drying stations by an unwind roll, located before coating station, and a rewind roll, located after the drying

station. Tension is applied to the substrate to ensure proper conveyance through the coating line *via* clockwise or counterclockwise torque at the unwind and rewind rolls. The conveyed speed of the substrate is controlled by a driven roller.

For R2R coating, the anode catalyst layers were coated onto a 125 µm thick ethylene–tetrafluoroethylene (ETFE) substrate. ETFE was used for two reasons: (1) it provides a very smooth coating surface and (2) the dried catalyst layer only weakly adheres to it enabling near 100% transfer of the catalyst layer to the membrane. The slot die and gravure coating equipment each consist of unique hardware used to apply a liquid coating of a desired wet thickness onto a substrate. For slot die coating, the die consists of an upstream die body, a downstream die body, and a shim which sits between the two die bodies (Fig. S2). The shim is a thin metal or plastic sheet which has been cut to provide a flow field between the two die bodies of fixed width. The gap between the die bodies is set by the thickness of the shim. For the present work, the die was shimmed to obtain an 80 mm wide coating width with a 254 µm die body gap. For these experiments the die geometry was fixed, and a vacuum box was not used. The catalyst ink was fed to the die using a syringe pump. For slot coating the film thickness (t) is determined by the flow rate of the coating fluid to the die ($\dot{Q}$), the substrate speed (U), and the coating width (w), as in eqn (1):

$$t = \frac{\dot{Q}}{Uw}. \qquad (1)$$

For gravure coating, various cylinders with different volume factors were used to obtain a range of liquid film thicknesses. All cylinders had a tri-helical pattern and details of the gravure cylinders used here are reported in the SI (Table S1). Coating was performed in direct-reverse-kiss coating mode, where the web is held over the gravure roll *via* tension and a coating is applied directly to the web *via* rotation of the gravure cylinder in the opposite direction to the web motion and a tangential speed of 1.5 m min^{-1}.

For all coatings prepared by slot die or gravure coating, the web speed was 1 m min^{-1}. The liquid films were dried in two 1-m long air floatation ovens with temperatures of 60 °C and 100 °C and air flows of 200 cubic feet per minute.

Spray coating

Spray-coated catalyst layers were fabricated by directly spraying the catalyst layer on to a Nafion 115 membrane. The cathode catalyst layer coated first, followed by the anode catalyst layer. Spray coating was performed using a Sono-Tek ExactaCoat ultrasonic spray system with a 25 kHz Accumist nozzle. The membrane was held in place using a vacuum plated heated to 80 °C.

MEA fabrication and testing

MEAs with R2R-coated catalyst layers were prepared by transferring the catalyst layers from the ETFE decal to a Nafion 115 (125 µm thick) membrane through a hot-pressing step. In this process the catalyst-coated decal and membrane were placed

between two sheets of polyimide film and 1/16″ thick Gylon. This stack was placed in a heated hydraulic press (125 °C) and pressed for 3 min at a pressure of 25 kg cm^{-2}, based on the area of the Gylon foam. These conditions result in 100% of the catalyst layer being transferred from the ETFE to the membrane. For all MEAs the cathode catalyst layers were spray coated on to the membrane, as described above, prior to transfer of the anode. A titanium porous-transport layer (Bekaert 2GDL10N-BSO2PT) that was coated with Pt by the manufacturer was used as the anode porous transport layer. The cathode gas diffusion layer (GDL) was carbon paper (AvCarb MGL280). The MEA active area was 5 cm^2, as defined by the PTFE gaskets used to seal the MEA into the testing hardware. The GDL thickness was compressed by approximately 20%. Cell components were dry-assembled in a custom electrolyzer test hardware using a triple-serpentine Ti flow fields coated with Pt for the anode side and Au for the cathode side.

MEA testing used the same conditioning and polarization curve protocol as previously described.[20] Electrolyzer cell tests were conducted using an in-house-constructed electrolyzer test station with a re-circulating water loop maintained at high purity with mixed-bed DI polishing resin. The anode was fed water at 80 °C and a flow rate of 50 mL min^{-1}, while the cathode was operated dry. The cell temperature was measured with a thermocouple inserted into the cathode flow field and regulated by heater pads placed on the hardware end plates. Before performance testing, all cells were conditioned using a combination of polarization curves and current/volage holds. Conditioning and durability testing used electrical power from the test station load bank. Polarization curves and impedance spectra were recorded using an Autolab potentiostat/galvanostat (PGSTAT302N, Metrohm) or Gamry potentiostat/galvanostat with a 20 A booster. For the polarization curves the cell voltage was measured at current densities from 10 mA cm^{-2} to 4 A cm^{-2} with roughly logarithmic spacing. Galvanostatic impedance spectra were recorded at every current density point and used to determine the high-frequency resistance by interpolating the real axis intercept. The AC amplitude for galvanostatic impedance measurements was maintained in the range of 1–5% of the DC current, with frequency range from 0.4 Hz to 40 kHz. Non-faradaic, transmission-line impedance curves were recorded potentiostatically at 1.25 V with a 3 mV rms amplitude and frequency range from 0.18 Hz to 18 kHz under a H$_2$/H$_2$O condition. The voltage cycling protocol to assess durability was a square wave cycle from 1.4–2.0 V, with a cycle time of 1 min for a total cycling time of 500 h. Polarization curves were recorded before and after cycling. During idle periods between durability testing and potentiostat diagnostics, the cell was held at 1.4 V to prevent depolarization leading to start/stop type degradation.

Catalyst layer and MEA analysis

The catalyst layer loadings were measured using an ambient X-ray fluorescence spectrometer (Fischerscope XDV-SDD). Optical microscopy was conducted using a Keyence VHX-5000 microscope with both transmitted and reflected illumination.

Cross-sectional scanning electron microscopy (SEM) images of coated anodes on the ETFE substrate were collected at 5000 magnification, with a Teneo LV SEM (Thermo Fisher Scientific, USA), using a circumferential backscattered (CBS) detector, an accelerating voltage of 10 kV and a beam current of 0.8 nA. The samples were prepared by embedding in the EpoThin epoxy resin (BUEHLER, USA), followed by polishing (Struers LaboPro-5, Denmark) and coating (Denton vacuum LLC, USA).

Cross-sectional scanning transmission electron microscopy with energy dispersive spectroscopy (STEM-EDS) was performed using a Talos F200X Thermo Fisher Scientific microscope, with an electron accelerating voltage of 200 kV. High-angle annular dark field (HAADF) images and EDS maps were collected at 40 000× magnification. The anode samples for TEM were prepared by embedding in a 1:1 mixture of trimethylolpropane triglycidyl ether resin (Sigma-Aldrich, USA) and 4,4′-methylenebis (2-methylcyclohexylamine, Sigma-Aldrich, USA) hardener, cured overnight, and sectioned by a Leica UCT ultramicrotome. The average catalyst aggregate sizes were measured using Local Thickness tool in Fiji Image J, as previously reported.[21]

Results

Rheology

Prior to coating, the steady shear viscosities of the inks were measured, as shown in Fig. 2. Poor coatings obtained at 10 wt% IrO$_2$ with a 1:1 ratio of water:1-propanol, however acceptable coatings were obtained by reducing the water content to a ratio
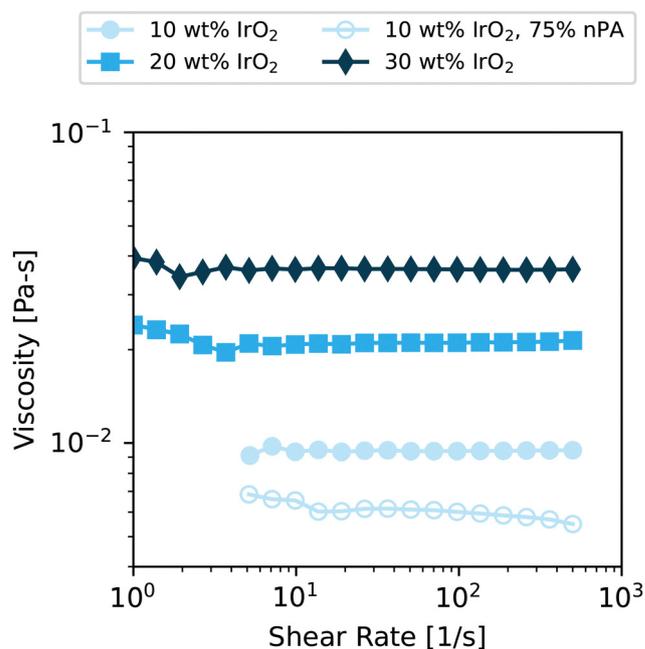

Fig. 2 Steady shear viscosities of catalyst inks measured with parallel-plate rheometry. Inks with 10 wt% IrO$_2$ inks were measured for dispersion media compositions of 50 wt% (filled symbol) and 75 wt% (open symbols) nPA. The 20 and 30 wt% IrO$_2$ inks had dispersion media compositions of 50 wt% nPA.

of 1 : 3. The viscosity profiles for both are shown. All inks display Newtonian rheology within the measured shear-rate range, There are some small increases in viscosity at share rates below 10 s^{-1} that we believe are due to torque sensitivity limits of the instrument and are unlikely to be indicative of shear-thinning. The trend of increased viscosity with increasing solids content is due to the increase in volume fraction of solids in the ink. The 1 : 3 water : 1-propanol ratio resulted in a slightly lower viscosity than a 1 : 1 ratio. Overall, these values are consistent with our prior measurements of IrO$_2$ inks.[22] The low viscosity at such a high wt% is due to the high density (11.66 g cm^{-3} for bulk IrO$_2$) and low porosity of IrO$_2$ leading to low volume fraction of solids in the inks in contrast to Pt/C catalyst particles, which have low density.[22]

Roll-to-roll coating

For R2R coating experiments the inks were then coated on to an ETFE substrate. First, we examined the coating window and loading ranges obtainable using slot die. Photographs of the coatings are shown in Fig. 3a. For all the inks coating defects can be observed for some of the coating conditions. The loadings resulting from the different coating conditions are plotted in Fig. 3b.

For the 10 wt% ink, very low loadings are obtainable given the low concentration of iridium in the ink. However, the uniformity of these coatings is poor. Due to the low surface tension and viscosity of this ink, the ink spread beyond the width of the shim (8 cm) to cover most of the substrate (10 cm wide) during application (bottom row in Fig. 3a). This spreading could be lessened by increasing the coating gap, however this is undesirable as it increases the likelihood of vortices that can lead to other coating defects.[6,23,24] This spreading leads to significant variation of catalyst loading across the width of the coating. For example, at a flow rate of 1.91 mL min^{-1}, the loading at the edge was 0.061 mg$_{Ir}$ cm^{-2} whereas it was 0.100 mg$_{Ir}$ cm^{-2} in the center, a 39% difference. Spreading also leads to the average loading being lower than the value predicted by eqn (1), because the coated width is larger than

targeted width set by the die body shim. Additionally, for 10 wt% ink coated at 7.63 mL min^{-1}, liquid leaked from the upstream side of the die onto the substrate, resulting in undesired streaks in the coated anodes (Fig. 3a). This streaking was present at higher flow rates and prevented the production of defect-free anodes with high loadings using the 10 wt% ink.

By increasing the ink concentration to 20 wt% IrO$_2$ a wider range of loadings could be obtained than at 10 wt% IrO$_2$. However, the lowest loading that could be obtained with this ink was 0.287 mg$_{Ir}$ cm^{-2} at 1.73 mL min^{-1}. Below this flowrate, defect-free coatings could not be obtained as the flow rates were below the low-flow limit, as shown by the image for the coating at 0.87 mL min^{-1} in Fig. 3. Below the low-flow limit, the upstream meniscus of the coating fluid recedes into the feed slot (see Fig. 1) and the coating bead becomes unstable and breaks giving rise to observed streaks.[6,25] While spreading still existed for the coatings with the 20 wt% ink, it was not as severe as with the 10 wt% ink and the loading at edge of the coating typically differed from the center by less than 10%.

For the 30 wt% ink, only high loadings could be obtained due to the high concentration of the ink. At a flow rate of 2.08 mL min^{-1}, a loading of 0.65 mg$_{Ir}$ cm^{-2} was obtained. This catalyst ink also resulted in improved control of the coating width, though there was still some spreading with the coated width being 85 mm wide, which was 5 mm wider than the shimmed width of 80 mm. This resulted in the loading being lower than predicted loading by eqn (1) (0.73 mg$_{Ir}$ cm^{-2}). Recalculating the predicted loading based on eqn (1) for the wider width leads to a predicted loading of 0.68 mg$_{Ir}$ cm^{-2}, which is in reasonable agreement with the measured loading. The edge was only 5% thinner than the center. Some center-to-edge variation is common in slot coating. Fluid flow velocity near the shim wall is typically reduced relative the flow velocity in the center of the slot due to drag imposed by shim wall. Since the fluid is Newtonian, this impact is small compared to highly non-Newtonian fluids thus the variation observed here is relatively small.[26] It is also possible the variation is due to nonuniform flow caused by the internal manifolding of the die,
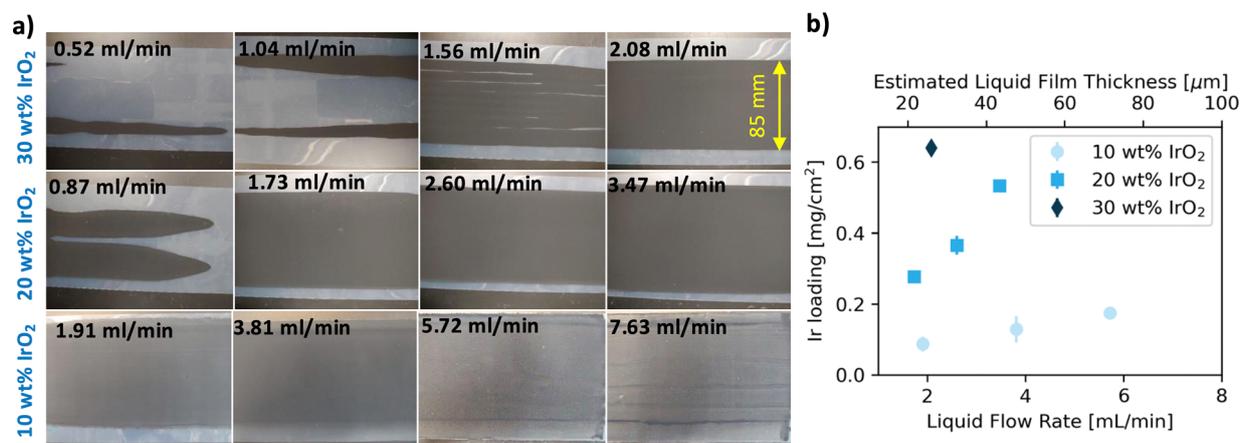

Fig. 3 (a) Photographs of slot-coated anode catalyst layers on EFTE for various liquid flow rates (indicated in upper left corner of each photograph). (b) Plot of measured Ir loading as a function of ink flowrate and estimated liquid film thickness (from eqn (1)).

which is known influence fluid flow uniformity.[24] The coating die used here is center fed with a small, straight chambered manifold roughly 2 cm from the slot exit, illustrated in Fig. S2. Because the manifold is relatively small, there may be a non-negligible pressure drop down the length of the chamber that results in a lower velocity at edges of the coating relative to the center. Other manifold and shim designs, such as the two-chamber manifolds,[27] the so-called coat-hanger manifold,[28] converging shims,[26] as well as other die designs[24] have been shown to increase cross-web flow uniformity. These manifolds are generally designed for a specific rheology to maximize uniformity. Further examination of this is beyond the scope of this report.

Decreasing the flow rate to 1.56 mL min^{-1} leads to coating with frequent voids in the coating indicating this flow rate was below the low-flow limit. We did not attempt to coat higher loadings, but based on prior experiments loadings of 1 mg$_{Ir}$ cm^{-2} are possible.[7]

For these experiments a vacuum box, commonly used to decrease the air pressure on the upstream side of the die and thus enable the low-flow limit to be reduced compared to the vacuum-free case, was not used.[29] The use of a vacuum box likely would have made it possible to coat thinner films and obtain lower loadings than we were able to obtain here. Additionally, changes in the die set up (slot width, upstream and/or downstream coating gap) would also likely influence flow limits. However, there are practical limits, as achieving very low loadings would require liquid films of only a few μm. At such low film thickness the coating gap must also be small, thus machining tolerances and roller or bearing eccentricity may make coating impractical for fear of damaging the die and backing roll through collision of the two. Additionally, very thin films are more susceptible to thickness nonuniformity due to machine vibrations than thicker liquid films. Tensioned web over slot die coating alleviates concerns of die damage since the substrate held against the die by tension instead of the backing roll, however this modality was not studied here.[23,30,31]

The same catalyst inks were used to prepare coatings using gravure coating. Here, we use direct gravure kiss coating where the fluid is transferred directly to the substrate without the use of an offset roll or backing roll.[32] In this work, the gravure cylinder was rotated in the opposite direction of the substrate, referred to as reverse gravure. Because the web is held in contact with the gravure cylinder by tension, the aforementioned concerns regarding machining tolerance in slot die coating are alleviated.

Seven gravure cylinders with different volume factors were used to achieve different liquid film thicknesses, and thus different loadings. The volume factors ranged from 24–170 cm^3 m^{-2}, which are predicted by the manufacturer to give liquid film thicknesses ranging from 4–9 μm for the lowest volume factor to 50–80 μm for the largest volume factor. A detailed list of the cylinders used is presented in Table S1 of the SI. The rotational speed was fixed at 1.5 m min^{-1} for all coatings based on past experiments that showed this speed resulted in stable coatings.[33] Images of the coatings are shown in Fig. 4a. The measured loadings as a function of volume factor are shown in Fig. 4b. With the combination of ink concentrations and cylinders we were able to obtain coatings with loadings from 0.06–0.57 mg$_{Ir}$ cm^{-2}. The lowest loading prepared is lower than we were able to prepare with slot die coating. This is not surprising as gravure coating is typically used with lower viscosity inks to produce thinner films than slot-die coating. However, at the lowest loadings the loading variation was higher than that observed at higher loadings, likely due to the liquid film thickness of a few μm approaching machining tolerances. It is likely we could have obtained higher loadings with a 30 wt% IrO$_2$ ink had we used the gravure cylinders with larger volume factors. In contrast to slot-die coating we do not observe significant cross-web variations in Ir loading.

Electron microscopy

We also used electron microscopy to understand the microscale uniformity of the catalyst layers. First, we imaged the coatings using SEM, as shown in Fig. 5. Images for a select set of catalyst layers were chosen to assess the impacts of different coating
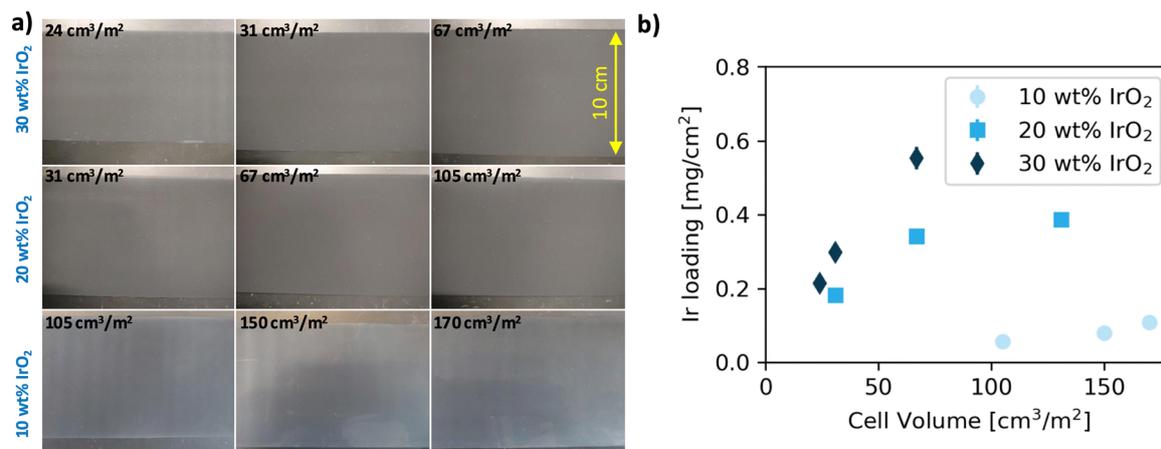

Fig. 4 (a) Photographs of gravure-coated anode catalyst layers on ETFE. Gravure cylinder cell volume factor is indicated in the corner of each photograph. (b) Plot of measured Ir loading as a function of gravure cylinder volume factor.
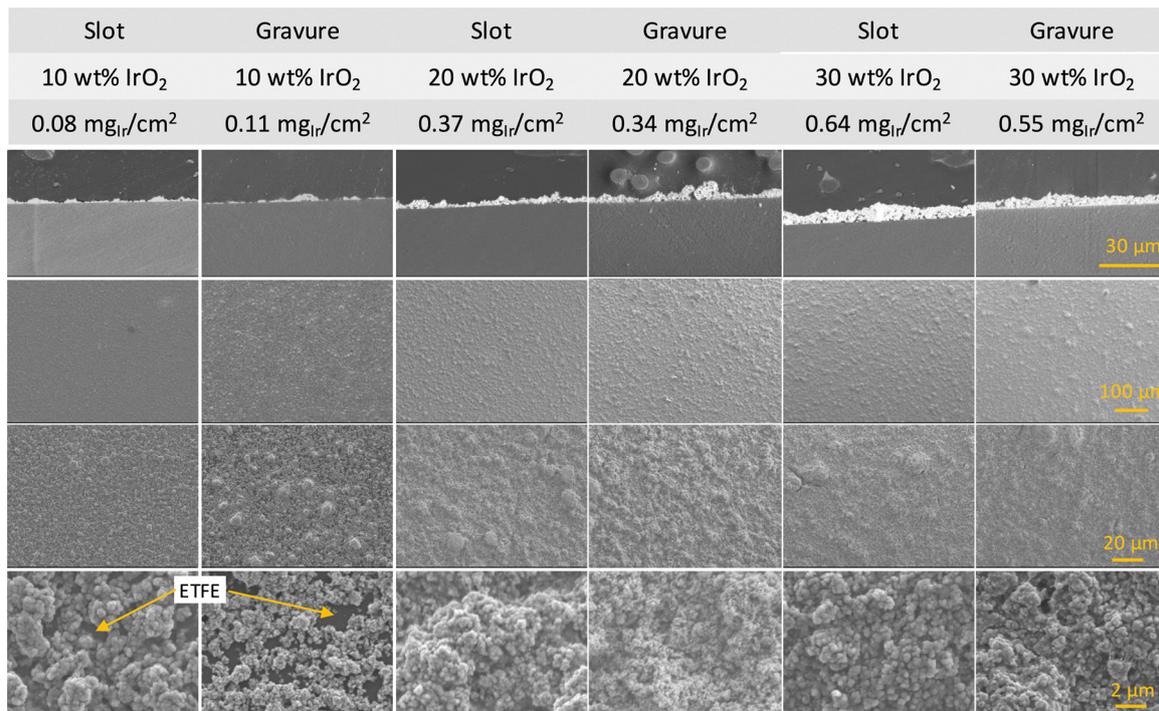
Slot	Gravure	Slot	Gravure	Slot	Gravure
10 wt% IrO$_2$	10 wt% IrO$_2$	20 wt% IrO$_2$	20 wt% IrO$_2$	30 wt% IrO$_2$	30 wt% IrO$_2$
0.08 mg$_{Ir}$/cm^2	0.11 mg$_{Ir}$/cm^2	0.37 mg$_{Ir}$/cm^2	0.34 mg$_{Ir}$/cm^2	0.64 mg$_{Ir}$/cm^2	0.55 mg$_{Ir}$/cm^2

Fig. 5 Cross-sectional SEM images (5000× magnification, row 1) and top-down SEM images (200×, row 2; 1000×, row 3; and 10 000×, row 4) of anode catalyst layer decals on ETFE.

parameters on microscale features of the catalyst layers. Images were acquired as cross sections and top down at three magnifications to determine features at varying length scales. From the cross-section a clear increase in thickness with increasing loading is apparent, as expected.

In the second and third rows, the top-down images show large clusters of catalyst protruding above the surface of the film. This is more pronounced in the gravure coated catalyst layer than the slot-die coated catalyst layer. We are unsure why the gravure coated catalyst layer has larger clusters compared to the slot-die coated catalyst layer. Interestingly, regardless of the ink concentration the gravure coated catalyst layers seem to have finer particulate size than slot die, which are visible at the highest magnification.

The cross-sections (top row) also show variations in thickness due to the clusters, consistent with the top-down images. The leftmost two columns contain images of catalyst layers with loadings near 0.1 mg$_{Ir}$ cm^{-2}. The cross-sectional images show discontinuities in the catalyst layers. The highest magnification top-down images (row 4) also show the films are discontinuous and the EFTE substrate is visible for both slot and gravure coating, as noted in the figure. For the 20 and 30 wt% IrO$_2$ coatings with loadings near 0.35 and 0.6 mg$_{Ir}$ cm^{-2} the cross sectional and top-down images show continuous catalyst layers. Catalyst agglomerates are still present.

The discontinuous nature of the low-loaded catalyst layers results from the IrO$_2$ primary aggregate size relative to the catalyst layer thickness.[22] Based on the highest loaded catalyst layers, we can estimate a thickness to loading ratio of 650 nm/ 0.1 mg$_{Ir}$ cm^{-2}. From our previous study on IrO$_2$ catalyst inks,

we have measured the hydrodynamic diameter of the catalyst aggregates to be around 240 nm.[22] Based on this size, a 0.1 mg$_{Ir}$ cm^{-2} catalyst layer of roughly 650 nm thick would be less than three catalyst aggregates thick. While densely packed layers of spheres are possible with monodispersed spheres under highly controlled conditions[34] such ordered packing is highly unlikely with irregularly sized and shaped catalyst particles coated using gravure and slot die coating. Furthermore, when the larger clusters are added to the consideration, it's clear that it is challenging to create low-loaded catalyst layers. Thus, it is not surprising that the low loaded catalyst layers are discontinuous. This suggests that for manufacturing of low-loaded catalyst layers, novel catalysts that increase layer thickness,[35–38] incorporation of conductive additives,[39] or alternative catalyst layer structures[40] are likely needed to improve catalyst layer homogeneity.

We also examined the nanoscale structure of the catalyst layers using scanning transmission electron microscopy (STEM). Shown in Fig. S3 are the high-angle annular dark field (HAADF) images and STEM-EDS elemental maps of the gravure and slot die samples with 30 wt% catalyst. The HAADF images (Fig. S3a and b) show a comparable structure of particles. Using the HAADF images we determined the average aggregate size for the gravure samples to be 225 ± 18 nm and for the slot die samples to be 218 ± 15 nm. These agree with the hydrodynamic diameter of roughly 240 nm measured by dynamic light scattering.[22] The STEM-EDS images in Fig. S3c and d show relatively similar distribution of iridium (red) and fluorine (green). The fluorine distribution indicates the ionomer

heterogeneously distributed and tends to agglomerate in certain areas.

Electrochemical testing

Using the anode catalyst layer decals, MEAs were prepared using a hot lamination (a.k.a. decal transfer) to Nafion 115 membranes. These MEAs were conditioned and tested at ambient pressure conditions. Polarization curves for gravure and slot coated catalyst layers with loadings near 0.4 mg_{Ir} cm^{-2} (20 wt% IrO_2 ink, see Fig. 5) as well a spray coated control sample are shown in Fig. 6. As can be seen in this Fig. 6(a), the polarization curves are nearly identical. There are some small differences at high current density that are more clearly visible in Fig. 6b, which plots the polarization curves between 3 and 4 A cm^{-2}. Here slight variations between the polarization curves are noticeable. Additionally, the HFR-free cell voltage (Fig. 6(c)) similarly shows only slight difference between samples of different coating method. This is also consistent with our past work on direct-coated catalyst layers that showed at 1 mg_{Ir} cm^{-2} the coating method did not significantly influence the polarization curves.[7] At 4 A cm^{-2} the difference between the lowest voltage (gravure, 2.066 V) and highest voltage (slot die, 2.080 V) is 14 mV. A previously published benchmarking study showed that intra-lab variance in uncorrected cell voltage was up to 12 mV suggesting the coating method is not impacting the initial performance.[41]

Nyquist plots of the impedance spectra measured at 0.1 and 1.0 A cm^{-2} are presented in Fig. S4. At 0.1 A cm^{-2} the spectra look relatively similar, with the most prominent difference being the gravure and slot die samples have a slightly wider arc than the spray coated sample. At 1.0 A cm^{-2} the gravure and slot die coated catalyst layers appear to have a small semicircular feature at high frequencies that is not present for the spray coated sample. These features are indicative that the catalyst layer resistance may be slightly higher (a few mΩ-cm^2) for the R2R-coated catalyst layers than the spray-coated catalyst layer.

To further compare the various catalyst layers prepared as part of this study we have plotted the HFR-free cell voltage at 0.1 and 4 A cm^{-2} for a variety of anode catalyst layer coating methods as a function of loading (with logarithmic scaling of the horizontal axis), as shown in Fig. 7a and b. Comparing the HFR-free cell voltage allows for better comparison of catalyst layers as it removes any influence of membrane thickness, cell test hardware, and lamination process. These plots do not show a significant influence of coating method or ink concentration on the HFR-free cell voltage as measurements at similar loadings have very similar performance, regardless of the coating method. There is a decrease in cell voltage as the loading is increased, as expected. To quantify the impact of loading we performed a linear regression analysis of the HFR-cell voltage data. The regression was performed with logarithmic scaling of the loading which gives a slope in mV per decade, allowing for comparison to Tafel kinetics. These lines of best fit are shown in gray in Fig. 7. From this regression analysis we measure that the HFR-free cell voltage decreases by 71 and 93 mV per decade of loading at 0.1 and 4.0 A cm^{-2}, respectively. For the MEAs
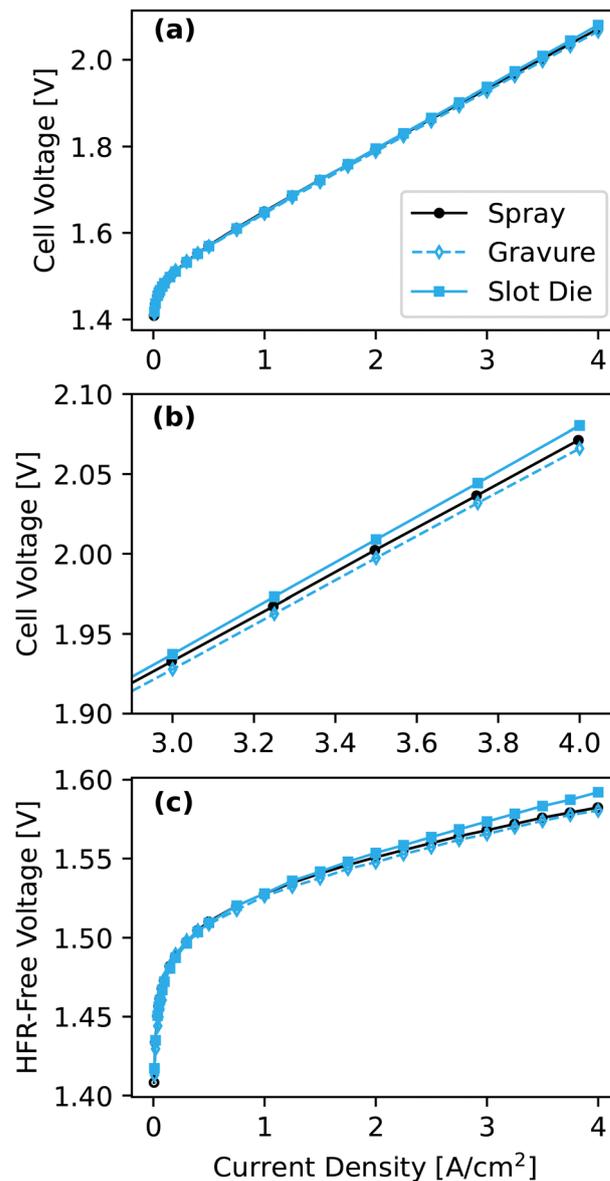

Fig. 6 (a) Polarization curves for MEAs with catalyst layers fabricated using slot die, gravure and spray coating. (b) Polarization curves from 3–4 A cm^{-2}. (c) High-frequency-resistance corrected polarization curves. All anodes have iridium loadings near 0.4 mg_{Ir} cm^{-2}.

measured in this study the mean Tafel slope was 50.5 mV per dec with a standard deviation of 2.76 mV per dec. Since the slopes of HFR-free voltage are greater than the Tafel slope it indicates a deviation from ideality likely due to heterogeneities in the catalyst layers as observed in Fig. 5. The decreased connectivity of the catalyst layer as loading decreases likely leads to an increase in electrode resistance or inactive particles, which has been shown to decrease utilization and increase the effective Tafel slope.[42] Additionally, as loading decreases the Tafel slope decreases by 9.0 mV per decade per mg_{Ir} cm^{-2}. This further indicates non-idealities in the catalyst layers.

In addition to testing MEAs for initial performance, we assessed the durability of MEAs with gravure- and spray-coated
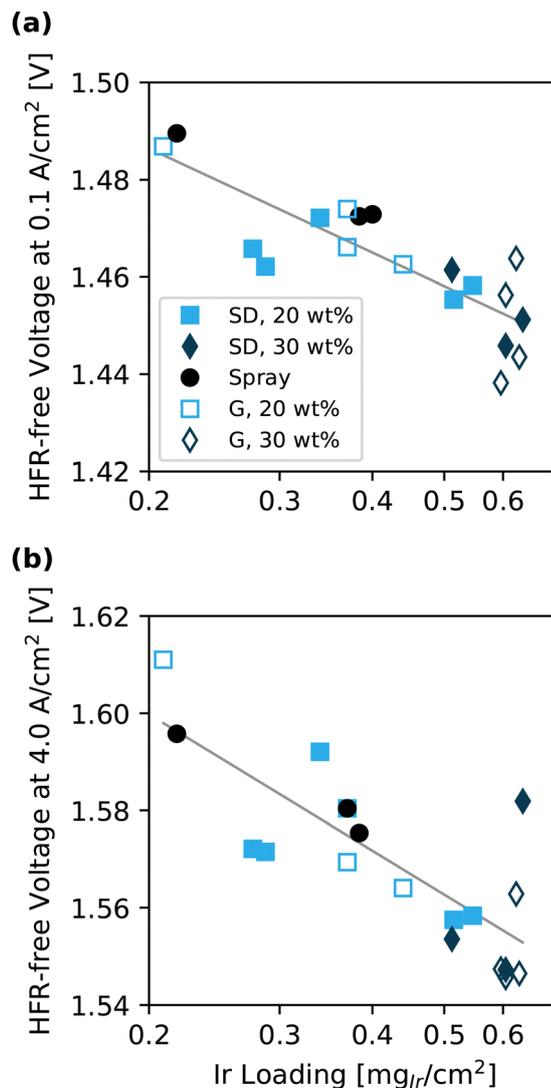
Fig. 7 Plots of HFR-free cell voltage ($V_{\text{HFR-free}}$) as a function of anode loading at current densities of (a) 0.1 A cm^{-2} and (b) 4.0 A cm^{-2}. The gray line is the line of best fit from linear regression analysis of these data.

catalyst layers with loadings of 0.2 and 0.4 mg$_{\text{Ir}}$ cm^{-2}. The MEAs were subjected to a 30 000 square-wave voltage cycle (1.4–2.0 V, 1 minute per cycle) durability test lasting 500 hours. Following cycling, final polarization curves were measured. The beginning-of-test (BOT) and end-of-test (EOT) polarization curves and HFR shown in Fig. 8a–d. HFR-free Tafel plots are shown in Fig. 8e and f. At both loadings these MEAs show only small differences in BOT performance, especially when HFR-corrected. The small difference in the HFR likely reflects the impacts of the lamination procedure on the membrane thickness and catalyst layer surface. After voltage cycling, the MEAs with 0.4 mg$_{\text{Ir}}$ cm^{-2} loaded catalyst layers show similar changes. The HFR-free polarization curves increase by similar amounts and maintain a similar shape, suggesting the degradation behavior is similar for both MEAs. For the spray-coated MEA the HRF-free voltage (Fig. 8e) increases by an average of 15 mV over all the measured current densities, with a range of 13–18 mV. For the gravure-coated MEA the average

increase is only slightly higher, 20 mV (18–22 mV), which may not be a statistically significant difference to the spray-coated MEA. faradaic and non-faradaic impedance spectra are shown in Fig. S6. They show changes between BOT and EOT, but difference between spray-coated and gravure-coated are small, consistent with polarization curve results.

Both 0.2 mg$_{\text{Ir}}$ cm^{-2} catalyst layers show greater degradation than those at 0.4 mg$_{\text{Ir}}$ cm^{-2}, consistent with prior results showing increasing degradation rates with decreased loading.[43] In contrast the results at 0.4 mg$_{\text{Ir}}$ cm^{-2}, at 0.2 mg$_{\text{Ir}}$ cm^{-2} the gravure-coated MEA shows greater average HFR-free voltage increase (Fig. 8f, mean: 43 mV, range 25–62) after cycling than the spray-coated MEA (Fig. 8e, mean: 0.29, range: 18–40 mV). While the EOT HFR-free voltages are nearly the same at lower current densities (below 0.1 A cm^{-2}), they are noticeably different at higher current densities. At current densities at and above 2 A cm^{-2}, the gravure-coated catalyst layer's HFR-voltage increases roughly 60 mV from BOT to EOT, whereas this increase is slightly less than 40 mV for the spray-coated catalyst layer. Similar trends are observed in EIS Nyquist plots shown in Fig. S6. At 0.1 A cm^{-2} the semicircle width increases by a similar amount for both coating methods, but at 1.0 A cm^{-2} the growth is much larger for the gravure coated MEA.

This increase at high current density is indicative of poor catalyst layer utilization in the gravure-coated catalyst layer, which may be indicated by the higher HFR-free voltage at high currents for this sample at BOT (Fig. 8f). We believe that the poor utilization of the 0.2 mg$_{\text{Ir}}$ cm^{-2} gravure-coated catalyst layer is due to poorer layer quality than the spray-coated catalyst layer at the same loading. Fig. S7, compares top-down images of the gravure and spray-coated catalyst layers at 0.2 and 0.4 mg$_{\text{Ir}}$ cm^{-2}. At loadings around 0.4 mg$_{\text{Ir}}$ cm^{-2} both spray coating and gravure coating produce continuous catalyst layers. As a result, the connectivity between catalyst particles should be high, leading to few, if any, areas of electronically isolated catalyst.[44] As a result, the stress on the catalyst will be distributed more evenly throughout the catalyst layer leading to lower degradation. At loadings near 0.2 mg$_{\text{Ir}}$ cm^{-2} spray-coating still produces a continuous catalyst layer. Like at 0.4 mg$_{\text{Ir}}$ cm^{-2}, the continuity of the catalyst layer will lead to the degradation being distributed more evenly throughout the catalyst layer. For the gravure coated catalyst layer there are noticeable discontinuities, similar those shown in Fig. 5 at 0.11 mg$_{\text{Ir}}$ cm^{-2}. The poor layer connectivity likely creates areas of the catalyst layer that are electronically isolated and thus electrochemically inactive. Therefore, the effective loading of the catalyst layer will be lower compared to the spray-coated catalyst layer, and only the active regions catalyst will be stressed leading to greater degradation for the gravure-coated catalyst layer than the spray coated catalyst layer. This is supported by non-faradaic, transmission line impedance measurements shown in Fig. S6. While the spray-coated catalyst layer shows the expected transmission line shape with a low slow region at high frequencies followed by a high slope region, the BOT and EOT gravure-coated catalyst layer spectra lacks a clear low or high slope region. Previous analysis of
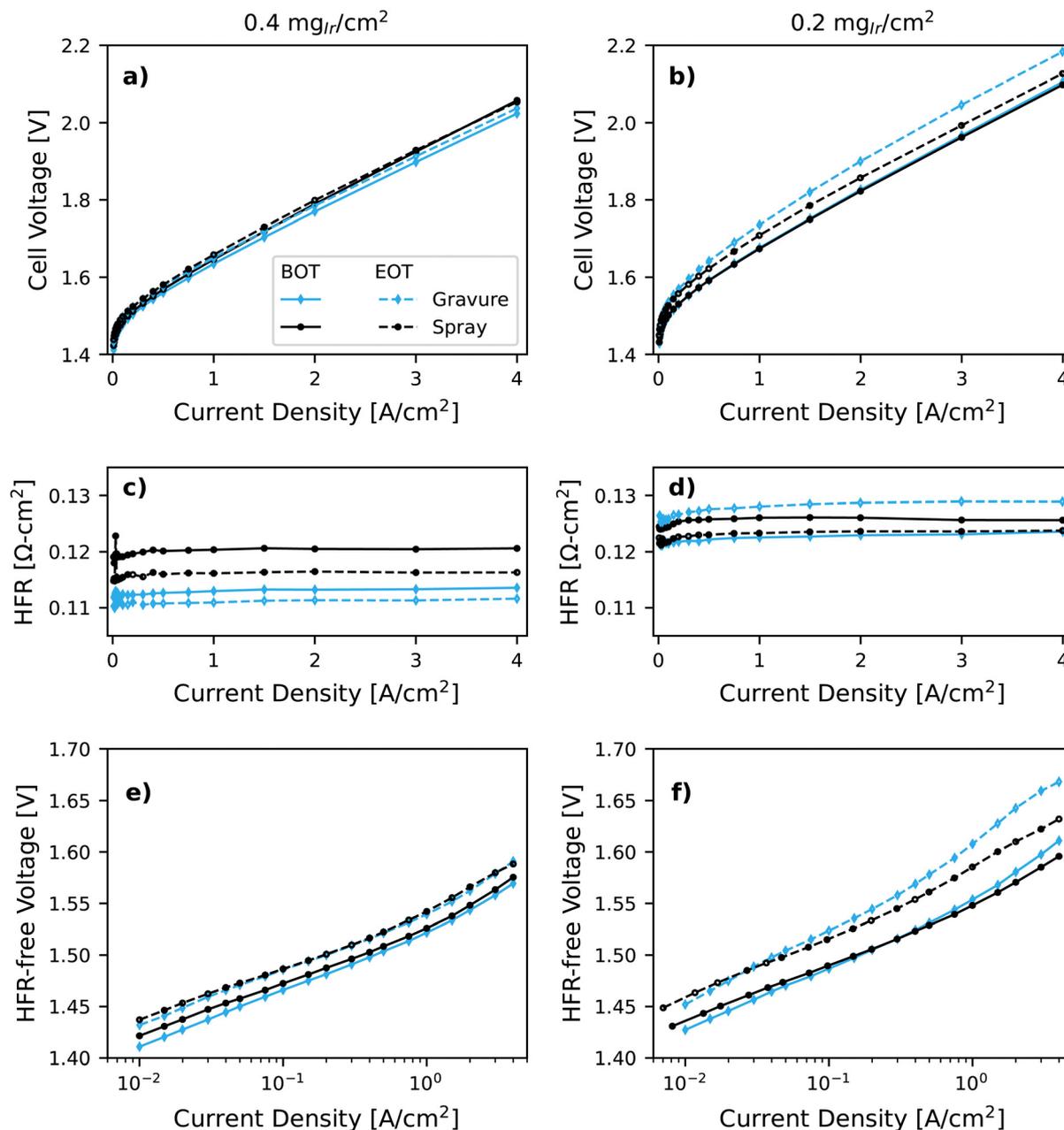
Fig. 8 Polarization curves of MEAs tested prior to (BOT) and following voltage cycling (EOT) for anode catalyst layer loadings of (a) 0.4 mg$_{Ir}$ cm^{-2} and (b) 0.2 mg$_{Ir}$ cm^{-2}. (c) and (d) BOT and EOT high-frequency resistance (HFR) of the tested MEAs. High-frequency-resistance corrected (HFR-free) plots of polarization curves before and after voltage cycling for anode catalyst layer loadings of (e) 0.4 mg$_{Ir}$ cm^{-2} and (f) 0.2 mg$_{Ir}$ cm^{-2}.

transmission line impedance spectra for Pt-black catalyst layers attributed similar behavior to heterogeneity in particle-to-particle contact and thickness nonuniformity, both of which are likely true for the gravure coated catalyst layer.[45]

To further explore our hypothesis of catalyst layer connectivity/utilization, we performed cross-sectional STEM imaging of catalyst layers at EOT (Fig. 9). As these images were acquired following potential cycling, all show an Ir band (dull gray circles) within the membrane directly adjacent to the catalyst layer (bright areas). In the lower magnification images (Fig. 9a and b) the catalyst layers with 0.4 mg$_{Ir}$ cm^{-2} loading

have Ir bands that are roughly the same thickness and of consistent thickness across the imaged region. The similarity of Ir band thickness between the two MEAs indicates similar dissolution of the catalyst, consistent with the potential cycling results.

Likewise, the images of the MEAs with 0.2 mg$_{Ir}$ cm^{-2} catalyst layers are also consistent with the potential cycling results. The spray-coated catalyst layer has an Ir band that has a uniform thickness (Fig. 9d and h). This supports our hypothesis that the high particle connectivity leads to dissolution that is uniformly distributed across the catalyst layer. As expected, the gravure-
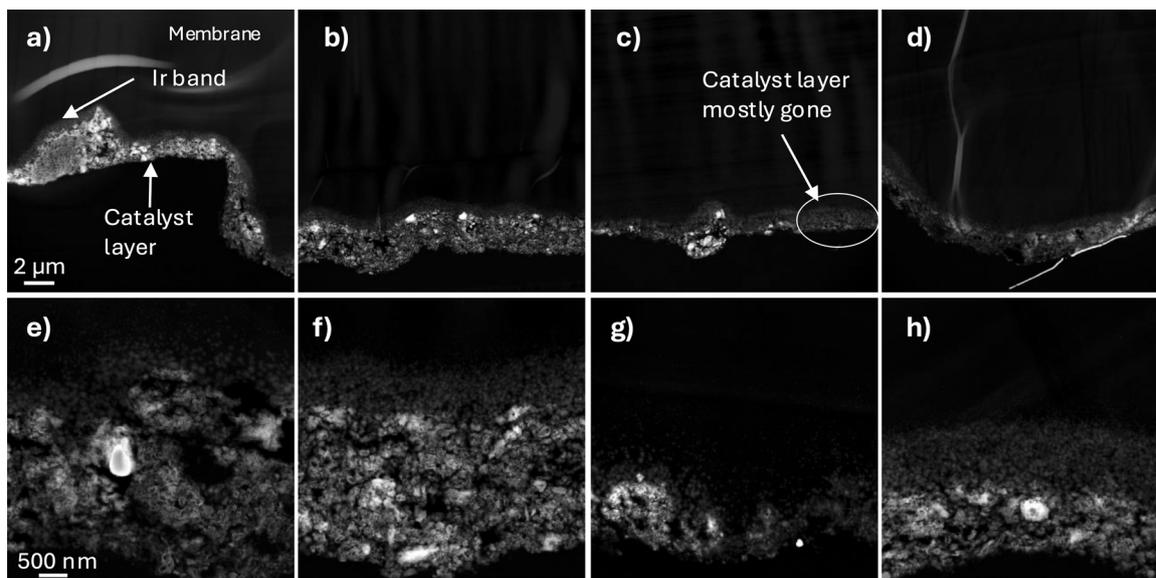
Fig. 9 High-angle annular dark field (HAADF) scanning transmission electron microscopy images of MEAs following 30 000-cycle square-wave potential cycling: (a) and (e) gravure coated, 0.4 mg_{Ir} cm^{-2}; (b) and (f) spray coated, 0.4 mg_{Ir} cm^{-2}; (c) and (g) gravure coated, 0.2 mg_{Ir} cm^{-2}; (b) and (f) spray coated, 0.2 mg_{Ir} cm^{-2}.

coated catalyst layer shows greater heterogeneity in both the catalyst layer and Ir band. In many areas the catalyst layer is no longer visible (lack of bright regions) and only the dull Ir band remains visible. This indicates in these areas the catalyst has been completely dissolved. This greater loss of catalyst is consistent with the greater voltage increase observed with potential cycling. These results clearly show that catalyst layers with high particle connectivity result in more durable catalyst layers.

Conclusion

This work shows that R2R slot-die and gravure coating can produce IrO_2 anodes at a range of loadings being targeted for future-generation electrolyzer systems. Due to the low viscosity of the catalyst inks used here, slot die coating shows lower cross-web uniformity than gravure coating due to spreading of the ink, however there are equipment designs that should be able to mitigate these issues. Additionally, formulation advancements that increase viscosity may also alleviate this problem.[46] More extensive investigation of slot-die coating parameters such as slot die gap or coating gap should be explored to more fully assess slot-die coatings suitability for low-loaded catalyst layers and improve uniformity. At moderate loadings around 0.4 mg_{Ir} cm^{-2} both methods produce layers with high continuity, and these layers show comparable performance (initially and after potential cycling) to layers produced using lab-scale spray coating. At loadings of 0.2 mg_{Ir} cm^{-2} and below, the dry catalyst layer films become discontinuous due to the similarities between agglomerate size and layer thickness. While these discontinuities were not found to impact initial performance to similarly loaded catalyst layers prepared using laboratory spray coating, after potential cycling

the R2R gravure-coated catalyst layers show greater performance loss than spray-coated anodes due to lower layer continuity which leads to lower catalyst utilization and to higher dissolution of catalyst in active areas. This finding suggests current iridium catalysts are not suitable to produce durable electrolyzers with low loadings. Thus continued developments in catalyst materials (*e.g.* iridium on or alloyed with other matals[35,47–49]) or catalyst layer structures that increase catalyst layer thickness while keeping Ir loading constant (*e.g.* incorporation of lower-coast metal,[39] nanowire structures[40,50]) are needed. As materials and catalyst layer structures evolve continued investigation of their manufacturability will be required to confirm whether promising lab-scale developments are translatable to roll-to-roll manufacturing methods.

Conflicts of interest

There are no conflicts to declare.

Data availability

Supplementary information contains photographs, tables, and graphics related to the equipment used in roll-to-roll coating, scanning electron microscopy of catalyst layers, electrochemical impedance spectra of electrolyzer MEAs, and Tafel slope analysis. See DOI: https://doi.org/10.1039/d5ya00309a.

Data from this project deemed appropriate for public access is available through the NLR Data Catalog, accessible at https://data.nrel.gov/submissions/303 (DOI: https://doi.org/10.7799/3003929). The NLR Data Catalog is the electronic catalog for data generated by federally funded research at NLR.

Acknowledgements

References

1 B. Pivovar, N. Rustagi and S. Satyapal, Hydrogen at Scale (H2@Scale): Key to a Clean, Economic, and Sustainable Energy System, *Electrochem. Soc. Interface*, 2018, **27**(1), 47–52, DOI: 10.1149/2.F04181if.

2 Hydrogen and Fuel Cell Technologies Office Multi-Year Program Plan; DOE/GO-102024-6266; Office of Energy Efficiency and Renewable Energy, 2024. https://www.energy.gov/eere/fuelcells/hydrogen-and-fuel-cell-technologies-office-multi-year-program-plan?utm_medium=email&utm_source=govdelivery.

3 C. R. Wang, J. M. Stansberry, R. Mukundan, H.-M. J. Chang, D. Kulkarni, A. M. Park, A. B. Plymill, N. M. Firas, C. P. Liu, J. T. Lang, J. K. Lee, N. E. Tolouei, Y. Morimoto, C. Wang, G. Zhu, J. Brouwer, P. Atanassov, C. B. Capuano, C. Mittelsteadt, X. Peng and I. V. Zenyuk, Proton Exchange Membrane (PEM) Water Electrolysis: Cell-Level Considerations for Gigawatt-Scale Deployment, *Chem. Rev.*, 2025, **125**(3), 1257–1302, DOI: 10.1021/acs.chemrev.3c00904.

4 A. Badgett, J. Brauch, A. Thatte, R. Rubin, C. Skangos, X. Wang, R. Ahluwalia, B. Pivovar and M. Ruth, *Updated Manufactured Cost Analysis for Proton Exchange Membrane Water Electrolyzers*, NREL/TP–6A20-87625, 2311140, MainId: 88400; 2024; p NREL/TP–6A20-87625, 2311140, MainId: 88400, DOI: 10.2172/2311140.

5 Z. Taie, X. Peng, D. Kulkarni, I. V. Zenyuk, A. Z. Weber, C. Hagen and N. Danilovic, Pathway to Complete Energy Sector Decarbonization with Available Iridium Resources Using Ultralow Loaded Water Electrolyzers, *ACS Appl. Mater. Interfaces*, 2020, **12**(47), 52701–52712, DOI: 10.1021/acsami.0c15687.

6 X. Ding, J. Liu and T. A. L. Harris, A Review of the Operating Limits in Slot Die Coating Processes, *AIChE J.*, 2016, **62**(7), 2508–2524, DOI: 10.1002/aic.15268.

7 J. Park, Z. Kang, G. Bender, M. Ulsh and S. A. Mauger, Roll-to-Roll Production of Catalyst Coated Membranes for Low-Temperature Electrolyzers, *J. Power Sources*, 2020, **479**, 228819, DOI: 10.1016/j.jpowsour.2020.228819.

8 M. Stähler, A. Stähler, F. Scheepers, M. Carmo and D. Stolten, A Completely Slot Die Coated Membrane Electrode Assembly, *Int. J. Hydrogen Energy*, 2019, **44**(14), 7053–7058, DOI: 10.1016/j.ijhydene.2019.02.016.

9 *Liquid Film Coating: Scientific Principles and Their Technological Implications*, ed. S. F. Kistler and P. M. Schweizer, Chapman & Hall, London, 1997.

10 R. Patel and H. Benkreira, Gravure Roll Coating of Newtonian Liquids, *Chem. Eng. Sci.*, 1991, **46**(3), 751–756, DOI: 10.1016/0009-2509(91)80181-W.

11 F. R. Pranchk and D. J. Coyle, Elastohydrodynamic Coating Systems, in *Liquid Film Coating*, ed. S. F. Kistler and P. M. Schweizer, Chapman and Hall, 1997.

12 R. W. Hewson, N. Kapur and P. H. Gaskell, A Theoretical and Experimental Investigation of Tri-Helical Gravure Roll Coating, *Chem. Eng. Sci.*, 2006, **61**(16), 5487–5499, DOI: 10.1016/j.ces.2006.04.021.

13 S. Khandavalli and J. P. Rothstein, Ink Transfer of Non-Newtonian Fluids from an Idealized Gravure Cell: The Effect of Shear and Extensional Deformation, *J. Non-Newtonian Fluid Mech.*, 2017, **243**, 16–26, DOI: 10.1016/j.jnnfm.2017.02.005.

14 J.-T. Wu, M. S. Carvalho and S. Kumar, Emptying of Gravure Cavities Containing Shear-Thinning and Shear-Thickening Liquids, *J. Non-Newtonian Fluid Mech.*, 2019, **268**, 46–55, DOI: 10.1016/j.jnnfm.2019.04.001.

15 E. B. Creel, K. Tjiptowidjojo, J. Alex Lee, K. M. Livingston, P. Randall Schunk, N. S. Bell, A. Serov and D. L. Wood III, Slot-Die-Coating Operability Windows for Polymer Electrolyte Membrane Fuel Cell Cathode Catalyst Layers, *J. Colloid Interface Sci.*, 2022, **610**, 474–485, DOI: 10.1016/j.jcis.2021.11.047.

16 M. S. Carvalho and H. S. Kheshgi, Low-Flow Limit in Slot Coating: Theory and Experiments, *AIChE J.*, 2000, **46**(10), 1907–1917, DOI: 10.1002/aic.690461003.

17 Y.-C. Huang, T.-Z. Wang, C.-P. Tsai and T.-J. Liu, Operating Window of Solution Casting, Part I: Newtonian Fluids, *J. Appl. Polym. Sci.*, 2013, **129**(1), 507–516, DOI: 10.1002/app.38617.

18 Y.-C. Huang, T.-Z. Wang, T.-J. Liu and C. Tiu, Operating Window of Solution Casting. II. Non-Newtonian Fluids, *J. Appl. Polym. Sci.*, 2015, **132**(5), 41411, DOI: 10.1002/app.41411.

19 R. Malakhov, K. Tjiptowidjojo and P. R. Schunk, Mechanics of the Low-Flow Limit in Slot-Die Coating with No Vacuum, *AIChE J.*, 2019, **65**(6), e16593, DOI: 10.1002/aic.16593.

20 E. Padgett, H. Yu, S. J. Blair, D. A. Cullen, R. K. Ahluwalia, D. J. Myers, B. Pivovar and S. M. Alia, Quantifying Sources of Voltage Decay in Long-Term Durability Testing for PEM Water Electrolysis, *J. Electrochem. Soc.*, 2025, **172**(5), 054508, DOI: 10.1149/1945-7111/add184.

21 C. M. Baez-Cotto, J. P. Pfeilsticker, A. O. Godoy, M. Batool, S. Zaccarine, M. Wang, O. Bird, S. Pylypenko, J. Jankovic, M. Ulsh and S. Mauger, The Effect of Ink Ball Milling Time on Interparticle Interactions and Ink Microstructure and Their Influence on Crack Formation in Rod-Coated Catalyst Layers, *J. Power Sources*, 2023, **583**, 233567, DOI: 10.1016/j.jpowsour.2023.233567.

22 S. Khandavalli, J. H. Park, N. N. Kariuki, S. F. Zaccarine, S. Pylypenko, D. J. Myers, M. Ulsh and S. A. Mauger, Investigation of the Microstructure and Rheology of Iridium Oxide Catalyst Inks for Low-Temperature Polymer Electrolyte Membrane Water Electrolyzers, *ACS Appl. Mater. Interfaces*, 2019, **11**(48), 45068–45079, DOI: 10.1021/acsami.9b14415.

23 J. Nam and M. S. Carvalho, Flow in Tensioned-Web-over-Slot Die Coating: Effect of Die Lip Design, *Chem. Eng. Sci.*, 2010, **65**(13), 3957–3971, DOI: 10.1016/j.ces.2010.03.032.

24 L. Sartor, *Slot Coating: Fluid Mechanics and Die Design*, University of Minnesota, 1990.

25 M. S. Carvalho and H. S. Kheshgi, Low-Flow Limit in Slot Coating: Theory and Experiments, *AIChE J.*, 2000, **46**(10), 1907–1917, DOI: 10.1002/aic.690461003.

26 G. L. Jin, W.-G. Ahn, S. J. Kim, J. Nam, H. W. Jung and J. C. Hyun, Effect of Shim Configuration on Internal Die Flows for Non-Newtonian Coating Liquids in Slot Coating Process, *Korea-Aust. Rheol. J.*, 2016, **28**(2), 159–164, DOI: 10.1007/s13367-016-0015-6.

27 K. J. Ruschak and S. J. Weinstein, Modeling the Secondary Cavity of Two-Cavity Dies, *Polym. Eng. Sci.*, 1997, **37**(12), 1970–1976, DOI: 10.1002/pen.11847.

28 Y. Matsubara, Geometry Design of a Coat-Hanger Die with Uniform Flow Rate and Residence Time across the Die Width, *Polym. Eng. Sci.*, 1979, **19**(3), 169–172, DOI: 10.1002/pen.760190302.

29 A. E. Beguin Method of Coating Strip Material. US2681294A, June 15, 1954. https://patents.google.com/patent/US2681294A/en?oq=US2681294A (accessed 2021-11-16).

30 D. J. Pipkin and D. W. Schaefer, *Method and Apparatus for Applying a Viscous Fluid to a Substrate*, US4299186A, 1981, https://patents.google.com/patent/US4299186A/en?oq=U.+S.+Patent+4%2c480%2c583, (accessed 2024-12-13).

31 Y. Tanaka and S. Noda, *Coating Apparatus*, US4480583A, 1984, https://patents.google.com/patent/US4480583A/en?oq=U.+S.+Patent+4%2c480%2c583, (accessed 2024-12-13).

32 H. Benkreira and R. Patel, Direct Gravure Roll Coating, *Chem. Eng. Sci.*, 1993, **48**(12), 2329–2335, DOI: 10.1016/0009-2509(93)80248-O.

33 S. A. Mauger, K. C. Neyerlin, A. C. Yang-Neyerlin, K. L. More and M. Ulsh, Gravure Coating for Roll-to-Roll Manufacturing of Proton-Exchange-Membrane Fuel Cell Catalyst Layer, *J. Electrochem. Soc.*, 2018, **165**(11), F1012–F1018, DOI: 10.1149/2.0091813jes.

34 P. Kumnorkaew, Y.-K. Ee, N. Tansu and J. F. Gilchrist, Investigation of the Deposition of Microsphere Monolayers for Fabrication of Microlens Arrays, *Langmuir*, 2008, **24**(21), 12150–12157, DOI: 10.1021/la801100g.

35 M. Möckl, M. F. Ernst, M. Kornherr, F. Allebrod, M. Bernt, J. Byrknes, C. Eickes, C. Gebauer, A. Moskovtseva and H. A. Gasteiger, Durability Testing of Low-Iridium PEM Water Electrolysis Membrane Electrode Assemblies, *J. Electrochem. Soc.*, 2022, **169**(6), 064505, DOI: 10.1149/1945-7111/ac6d14.

36 S. Zargarian, C. Roiron, G. Ferro and P. Atanassov, Iridium Oxide Network on Non-Conductive TiO2 Support as a Catalyst for Oxygen Evolution Reaction, *ChemElectroChem*, 2025, **12**(8), e202400625, DOI: 10.1002/celc.202400625.

37 B. M. Tackett, W. Sheng, S. Kattel, S. Yao, B. Yan, K. A. Kuttiyiel, Q. Wu and J. G. Chen, Reducing Iridium Loading in Oxygen Evolution Reaction Electrocatalysts Using Core–Shell Particles with Nitride Cores, *ACS Catal.*, 2018, **8**(3), 2615–2621, DOI: 10.1021/acscatal.7b04410.

38 M. Bernt, A. Hartig-Weiß, M. F. Tovini, H. A. El-Sayed, C. Schramm, J. Schröter, C. Gebauer and H. A. Gasteiger, Current Challenges in Catalyst Development for PEM Water Electrolyzers, *Chem. Ing. Tech.*, 2020, **92**(1–2), 31–39, DOI: 10.1002/cite.201900101.

39 K. J. Ferner and S. Litster, Composite Anode for PEM Water Electrolyzers: Lowering Iridium Loadings and Reducing Material Costs with a Conductive Additive, *ACS Appl. Energy Mater.*, 2024, **7**(18), 8124–8135, DOI: 10.1021/acsaem.4c01866.

40 F. Hegge, F. Lombeck, E. Cruz Ortiz, L. Bohn, M. von Holst, M. Kroschel, J. Hübner, M. Breitwieser, P. Strasser and S. Vierrath, Efficient and Stable Low Iridium Loaded Anodes for PEM Water Electrolysis Made Possible by Nanofiber Interlayers, *ACS Appl. Energy Mater.*, 2020, **3**(9), 8276–8284, DOI: 10.1021/acsaem.0c00735.

41 T. Lickert, S. Fischer, J. L. Young, S. Klose, I. Franzetti, D. Hahn, Z. Kang, M. Shviro, F. Scheepers, M. Carmo, T. Smolinka, G. Bender and S. Metz, Advances in Benchmarking and Round Robin Testing for PEM Water Electrolysis: Reference Protocol and Hardware, *Appl. Energy*, 2023, **352**, 121898, DOI: 10.1016/j.apenergy.2023.121898.

42 D. Y. Chung, S. Park, P. P. Lopes, V. R. Stamenkovic, Y.-E. Sung, N. M. Markovic and D. Strmcnik, Electrokinetic Analysis of Poorly Conductive Electrocatalytic Materials, *ACS Catal.*, 2020, **10**(9), 4990–4996, DOI: 10.1021/acscatal.0c00960.

43 S. M. Alia, S. Stariha and R. L. Borup, Electrolyzer Durability at Low Catalyst Loading and with Dynamic Operation, *J. Electrochem. Soc.*, 2019, **166**(15), F1164, DOI: 10.1149/2.0231915jes.

44 M. Bernt, A. Siebel and H. A. Gasteiger, Analysis of Voltage Losses in PEM Water Electrolyzers with Low Platinum Group Metal Loadings, *J. Electrochem. Soc.*, 2018, **165**(5), F305, DOI: 10.1149/2.0641805jes.

45 E. L. Thompson and D. Baker, Proton Conduction on Ionomer-Free Pt Surfaces, *ECS Trans.*, 2011, **41**(1), 709–720, DOI: 10.1149/1.3635605.

46 S. Khandavalli, J. H. Park, R. Rice, D. Y. Zhang, S. A. Berlinger, G. Bender, D. J. Myers, M. Ulsh and S. A. Mauger, Aging Iridium Oxide Catalyst Inks: A Formulation Strategy to Enhance Ink Processability for Polymer Electrolyte Membrane Water Electrolyzers, *Soft Matter*, 2024, **20**(45), 9028–9049, DOI: 10.1039/D4SM00987H.

47 M. Bernt and H. A. Gasteiger, Influence of Ionomer Content in IrO2/TiO2 Electrodes on PEM Water Electrolyzer Performance, *J. Electrochem. Soc.*, 2016, **163**(11), F3179–F3189, DOI: 10.1149/2.0231611jes.

48 X. Lyu, H.-M. Chang, H. Yu, N. N. Kariuki, J. Hyung Park, D. J. Myers, J. Yang, I. V. Zenyuk and A. Serov, Evaluation of IrO2 Catalysts Doped with Ti and Nb at Industrially Relevant Electrolyzer Conditions: A Comprehensive Study, *Chem. Eng. J.*, 2025, **505**, 159317, DOI: 10.1016/j.cej.2025.159317.

49 D. Böhm, M. Beetz, C. Gebauer, M. Bernt, J. Schröter, M. Kornherr, F. Zoller, T. Bein and D. Fattakhova-Rohlfing, Highly Conductive Titania Supported Iridium Oxide Nanoparticles with Low Overall Iridium Density as OER Catalyst for Large-Scale PEM Electrolysis, *Appl. Mater. Today*, 2021, **24**, 101134, DOI: 10.1016/j.apmt.2021.101134.

50 A. Steinbach, *Advanced Manufacturing Processes for Gigawatt-Scale Proton Exchange Membrane Water Electrolyzers*, 2024.